Express Polymer Letters Vol.17, No.6 (2023) 596–609
Available online at www.expresspolymlett.com
https://doi.org/10.3144/expresspolymlett.2023.44

Research article

Polyethylene terephthalate track etched membrane for recovery of helium from helium-nitrogen system

Bipin Chandra Nailwal[1], *Nitesh Goswami*[1], *Jayprakash P. Nair*[2], *Biju Keshavkumar*[3], *Puthiyedath Surendran*[2], *Anit Kumar Gupta*[2], *Soumitra Kar*[1,4*], *Asis Kumar Adak*[1]

[1]Desalination & Membrane Technology Division, Bhabha Atomic Research Centre, Trombay, 400085 Mumbai, India
[2]Nuclear Physics Division, Bhabha Atomic Research Centre, Trombay, 400085 Mumbai, India
[3]Health Physics Division, Bhabha Atomic Research Centre, Trombay, 400085 Mumbai, India
[4]Homi Bhabha National Institute, Anushakti Nagar, 400094 Mumbai, India

Received 4 October 2022; accepted in revised form 4 January 2023

Abstract. In this work, for the first time, the authors report polyethylene terephthalate (PET) track-etched membrane fabrication and detailed quantitative parametric studies for its application in He–N_2 separation. The study also covers theoretical studies to understand the irradiation of PET film with ions as well as the contribution of gas flow domains, which is attempted for the first time. Monte Carlo simulations were carried out using the FLUKA code to evaluate the dose deposited by the ions in the PET film and the displacement per atom (DPA). The distribution of absorbed dose in the film as a function of thickness, the mean absorbed dose as a function of ion energy, and DPA at various depths in the film was determined using these simulations. The range of various ion beams was also calculated using the SRIM code. The effect of incident energy of irradiation beam (Si: 70 and 90 MeV and Cl: 84, 100 and 115 MeV) and etching parameters like concentration of NaOH, temperature, UV radiation, and ultrasonication on the control and irradiated polymer films (~25 µm thickness) were studied. Gas permeation studies of in-house synthesized track etched membrane (optimum) were carried out and a promising He/N_2 selectivity of ~2.4 was achieved. The results confirmed that the membranes can have a potential application in the separation of He from natural gas.

Keywords: *polymer membranes, tailor-made polymers, modelling and simulation, thermal properties, track etched membrane*

1. Introduction

Helium has significant applications in fields of science, medicine, and industry because of its very low boiling temperature and chemically inert nature [1, 2]. It is used as a coolant in magnetic resonance imaging (MRIs), an inert gas in welding, a carrier gas in analytical and scientific equipment, helium/oxygen mixtures for deep-sea scuba divers, and in pressurizing and purging of pressure vessels, such as in rocket technology [1, 3].

The major source of helium is a natural gas field, mainly in the USA, where helium concentrations in natural gas can be up to 4 mol% [2, 4]. Natural gas consists of 30–90% of methane with light hydrocarbons depending on resource location. The process of He recovery from natural gas includes a pre-treatment process for removing acid gases, water, and heavy metals, the liquid natural gas (LNG) production process to recover natural gas, and a nitrogen rejection unit (NRU) in which N_2 is separated from off-gas from the LNG production unit. Conventional helium recovery and purification is done directly from the natural gas or the off gas from the NRU of a traditional natural gas processing plant [5], the latter being a more feasible option. The technologies used for helium recovery are membranes, pressure

---

[*]Corresponding author, e-mail: soubiswa@barc.gov.in

swing adsorption (PSA), and cryogenic technique [6]. Membrane technology, being cost-effective, simple to install, low maintenance, environment-friendly, and easy to scale up, has greater acceptability [7–13]. Membranes are used in various gas separation applications, like the separation of C_2–C_4 olefins from nitrogen in petroleum plants [14], nitrogen or volatile component from the air [15], hydrogen sulfide from methane [16], volatile organic compounds (VOCs) from the air [17], oxygen enrichment [18], and air dehydration acid gases such as hydrogen sulfide and carbon dioxide from methane [19]. Cellulose acetate (CA) membranes have been studied for helium separation and their hydrogen permeability was found to be around 14 barrer [20]. Cu-BDC (where BDC^{2-} = 1,4-benzenedicarboxylate) nanosheets blended polyimide mixed matrix membranes for helium separation were developed and found to be highly selective for He [21]. Density functional theory (DFT) calculations and molecular dynamic (MD) simulations of 2D graphitic carbon oxide have shown that these membranes are selective for He [22].

Generally, the dense membranes of polysulfone, polyetherimide, and polyimide are used for gas separation through a solution diffusion mechanism [23–25]. However, in the case of porous membranes, viscous transport and Knudsen diffusion are the main mechanisms of gas permeation. The viscous transport takes place when the pore diameter is higher compared to the mean free path of the gas molecules. The permeability of porous membrane is governed by viscous flow is given by Equation (1):

$$\text{Permeability} = c\varepsilon r^2 \tag{1}$$

where ε is the porosity, c is the geometric factor that accounts for the shape, connectivity, aspect ratio of pores, and tortuosity of the pores, and r is the pore radius (in metres). Knudsen diffusion takes place when the pore size is larger than the molecule size but smaller than the mean free path of the gas molecule. In this regime, collisions between gas molecules and the pore wall are dominant over the collisions between the gas molecules themselves. Gas transport by Knudsen diffusion occurs in the gaseous state without any adsorption because the interaction between diffusing molecules and the pore wall is negligibly small [26–28]. The permeability of porous membrane governed by Knudsen diffusion is given by Equation (2):

$$\text{Permeability} = 2\frac{\varepsilon\eta r v}{3RT} \tag{2}$$

where, η is the viscosity, r is the pore radius, R is the universal gas constant, T is the temperature and v is the molecular velocity given by Equation (3):

$$v = \sqrt{\frac{8RT}{\prod M}} \tag{3}$$

where M the is molecular weight of the gas.

A uniform pore size is a crucial requirement of membranes to get a good separation in the case of porous membranes. Pores generally have irregular shapes and cage-like/spherical mesoporous structures [19, 28–32]. Track-etched membranes are a good alternative for gas separation applications, as they offer very narrow pore size distribution [33, 34]. The track-etched membranes are polymer films in which pores are formed by etching the polymeric films after irradiation with high-energy particles. During etching, the polymer degraded during irradiation is etched out and a narrow pore size distribution is obtained in comparison to the membranes fabricated by other methods [35]. Hence, these membranes have note-worthy applications in gas separation [36], medical [37], nano-wire production [38], and biomedical industries [39]. Polycarbonate (PC), polyethylene terephthalate (PET), polypropylene (PP), polyvinylidene fluoride (PVDF), and polyimides (PI) are good candidate materials for fabricating track etched membranes, as ion track pores with high aspect ratio can be produced in theses polymer films. In the case of PC and PET mostly alkaline etching is used, while in the case of PP and PVDF, strong oxidizers can be used for etching. The etching of PI is a difficult task due to its stability at high temperatures. A mixture of NaOCl and H_2O_2 can be used for the etching of the PI membrane. Krypton ions [40], uranium fission products, xenon ions, and deuterium ions [41] are generally used for the irradiation of polymer films. PET polymer has good resistance towards acids, and hence acid-based etching of PET irradiated polymers is usually not considered. As the etching resistance of PET towards bases is low, a basic etchant is used for the etching of PET films. In PET film, the partially charged ester group gets hydrolyzed by an alkaline solution, which breaks the bonds between carbon and oxygen during etching, resulting in pore formation in the irradiated polymer film [42]. A disadvantage of using PET membrane is its susceptibility to hydrolysis in the presence of water vapors [43, 44].

In the present study, PET track etched membrane was synthesized using Si-28 and Cl-35 ions as irradiation beam and NaOH as etching media. Parametric studies involving etchant concentration, etching time, temperature, UV irradiation, and ultrasonication were carried out, and optimization of etching conditions was done. Modeling and simulation studies of the effect of radiation on the membrane was studied using the FLUKA code. The samples were characterized by scanning electron microscope (SEM), atomic force microscope (AFM), thermogravimetric analyzer (TGA), and differential scanning calorimeter (DSC). The gas permeation studies of track-etched membranes were carried out for the separation of helium from nitrogen. In this work, for the first time, the authors report a detailed and quantitative parametric study for the fabrication of PET track etched membrane, its testing for helium-nitrogen separation, along with theoretical studies in order to understand irradiation of PET film with ions as well as the contribution of gas flow domains towards observed permselectivity for helium.

2. Experimental

2.1. Irradiation of PET film

PET film (ultimate tensile strength: 170 MPa, bursting strength: 0.45 MPa, ultimate elongation: 120%, thickness: 25 µm, and density: 1.395 g/cm^3) was procured from M/s Garware Polyesters, India. Figure 1a shows the schematic of the irradiation setup. The magnetic beam scanner is an AC magnet, powered by AC mains (230 V, 15 A). The 50 Hz line frequency is used to scan the beam horizontally. The ions (beam) were deflected in one direction during the upward cycle and in the opposite direction during the downward cycle of AC. In every cycle, the beam was scanned from left to right and vice versa once. The deflection at the end of the magnet is of few cm. As the distance from the magnet increases, the deflection increases proportionally. To accommodate the large deflection, a horn chamber was used. The vertical distribution of ions was carried out by moving the film in a vertical direction using a rolling mechanism. The horn chamber is 1 m long and 50 cm wide. It could accommodate a 45 cm wide film for irradiation. The chamber has a rolling mechanism to move the film vertically. The film was wound on stainless steel rod (10 mm diameter and 45 cm long) supported at the ends of ball bearings. These rods were rolled using a DC motor via vacuum rotary feed-through.

PET film ~25 µm thickness was irradiated with Si-28 and Cl-35 beams of various energies at a particle flux of $6.2\cdot10^9$/sec at BARC-TIFR Pelletron Accelerator (Figure 1b). Heavy ions were produced using a Source of Negative Ions by Cesium Sputtering (SNICS). SiC was used as the source of Si ions and AgCl for Cl beams. Desired ions were selected using a mass analyzer magnet and injected into the pelletron accelerator. Negative ions from the ion source were accelerated towards the terminal and converted into positive ions using a carbon foil stripper. Multiply charged states were produced in various proportions depending upon terminal voltage. The desired energy of ions was obtained by selecting the terminal voltage and suitable charge state given by the formula in Equation (4):

$$E = V(q+1) \tag{4}$$

where E is the energy in eV , V is the terminal voltage of the accelerator in Volts, and q is the charge state. Different charged states had different energies for the same terminal voltage, and desired energy

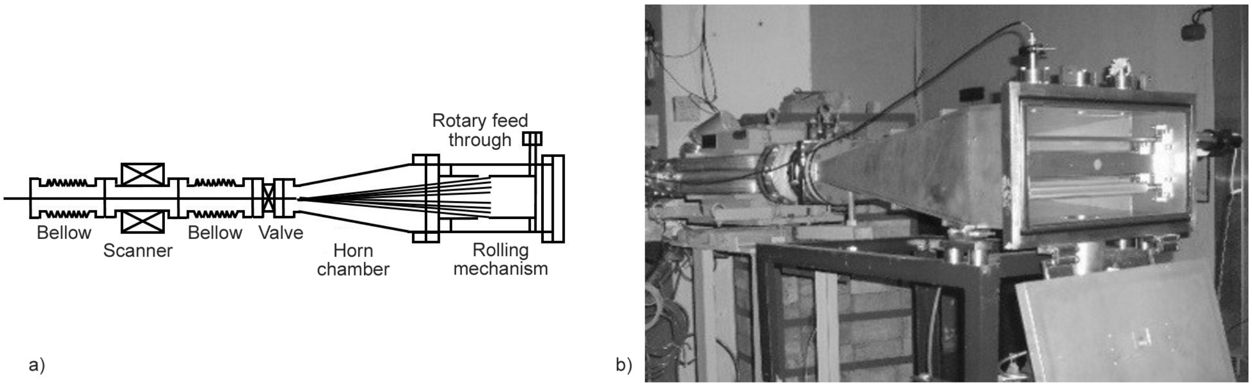

Figure 1. a) Schematic of irradiation setup, b) Indigenously developed setup for irradiation of polymer films.

was selected by using an energy-analyzing magnet. These ions were further stripped for higher charge states using a post-stripper. Among the multiple charges formed in the post-stripper, the highest charge state of reasonable yield was selected using a switching magnet for irradiation. The higher charge for a given energy gives wider deflection when the beam is scanned on the PET film. The beam was scanned on PET film by a magnetic scanner to achieve horizontal scanning. Vertical scanning was done by moving the film in a vertical direction using a geared DC motor and rotary vacuum feedthrough. The linear speed of the film was kept at 40 cm/min. Scan width and film length per unit time give the area of irradiation per unit time. Controlling the ion flux in that given time provides the desired pore density. The pore size was determined by the energy loss of ions while passing through the film. The higher the energy loss (which is a function of the atomic number (Z)), the larger the pores formed. The entire irradiation setup is functional at BARC-TIFR Pelletron Accelerator Facility. The irradiated films were cut, and etching studies were carried out.

2.2. Etching rate determination of PET film

During etching, both unirradiated and irradiated polymer films were placed in an alkaline solution (NaOH, Merck). The weights of the irradiated and unirradiated films were taken before the start of the etching process. The effect of ultrasonication was studied by keeping the sample in an ultrasonication bath (LAB MAN Scientific Instruments, LMUC-2). The ultrasonicator was operated at a frequency of 40 kHz, and a power of 50 W. Etching rate was determined with different concentrations (3, 6, 8, and 10 N) of NaOH at different temperatures (40, 50, 60, and 70 °C) with/without ultrasonication and UV (Chemito, India) irradiation at ~400 nm. It was calculated by Equation (5):

$$\text{Etching rate of polymer} = \frac{w_\mathrm{i} - w_\mathrm{f}}{w_\mathrm{i} t} \quad (5)$$

where w_i is the initial weight of the polymer in g, w_f is the final weight of the polymer in g, t is the etching time in minutes. The etching of the sample was carried out in reflux mode to avoid the change in concentration of the etching bath. The control and the etched membranes were characterized by SEM (Zeiss evo18), AFM (NT-MDT-Multimode 3, Ireland), TGA, and DSC techniques (Mettler-Toledo AG (MTANA), Switzerland). TGA and DSC analyses were carried out in a nitrogen gas atmosphere with a gas flow rate 50 ml/min at a heating rate of 10 °C/min. The analysis was carried out in the temperature range of 50–600 °C.

2.3. Pure water permeation studies

Pure water permeation studies of track-etched membranes were carried out at room temperature. The film was exposed to the water, and a steady-state permeate flow rate was measured. The pressure of the feed side was maintained at 1 bar.

2.4. Gas permeation studies

The gas permeation studies of membranes etched under an optimized set of conditions were carried out with individual gases of helium (He) and nitrogen (N_2) at room temperature in a dead-end mode. The pressure of the feed side was maintained at a particular value, and the corresponding flux of gas was measured. Figure 2 shows a pictorial representation of the gas permeation setup. P1 is the absolute downstream pressure, and P2 is the feed side absolute pressure [Pa]. Flux and selectivity of the membrane were calculated using Equations (6) and (7), respectively:

$$F = \frac{Q}{A} \quad (6)$$

$$\alpha_\mathrm{e} = \frac{\text{Permeance}_\mathrm{He}}{\text{Permeance}_{\mathrm{N}_2}} \quad (7)$$

where F is the flux of gas through the membrane, Q is the flow rate of gas through the membrane, A is the cross-section area of the membrane, α_E is the selectivity of the membrane calculated from experimental flux.

The membranes were tested for flux and selectivity in a mixed gas environment using a calibration gas mixture of 20% He and 80% N_2. The composition of

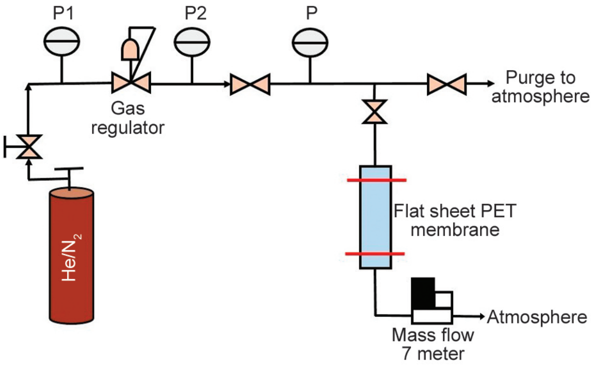

Figure 2. Pictorial representation of gas permeation setup.

the mixed gas was analyzed using Quadrupole Mass Spectrometer.

2.5. Characterization of membrane

The membranes were characterized by their surface roughness, pore size and thermal stability. The surface roughness of the membrane was determined by atomic force microscopy (AFM, NT-MDT-Multimode 3, Ireland) for a sample area of 10×10 µm. The pore size of the membrane was determined using scanning electron microscopy (SEM, Oxford Instrument, Zeiss Evo 18) at a voltage of 20 kV and magnification of 15 000×. SEM and AFM images were analyzed with ImageJ software to determine the pore size of the membrane. While analyzing the samples with AFM, larger pores formed due to pore mergers have not been considered. For thermal stability, membranes were analyzed using TGA and DSC analysis. To study the effect of radiation on the membrane, the relative crystallinity of samples was analyzed using X-ray diffraction (XRD, GNR Analytical Instruments, Italy).

3. Modeling and simulation studies

3.1. Dose deposition studies using Monte Carlo simulations

Monte Carlo simulations were carried out using FLUKA code (2021.2.0) [45]. The ion beam was incident normally on a PET film of 45 cm width, 0.33 cm breadth, and 25 µm thickness. The simulated geometry is shown in Figure 3. The dose deposited by the ions in the PET film (25 microns thick) and the displacement per atom (DPA) in the film were evaluated.

3.2. Permeance and theoretical selectivity

The permeance of gas was calculated using Equation (8):

$$\text{Permeance} = \frac{F}{P} \tag{8}$$

where F is the flux of gas and P is the partial pressure difference.

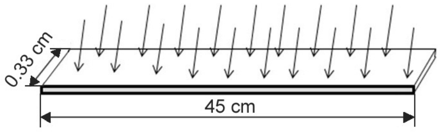

Figure 3. The simulated geometry in FLUKA code.

The flux of gas through the membrane is inversely proportional to the square root of the molecular weight of the gas in the case of Knudsen diffusion flow. The theoretical selectivity of the membrane was calculated by Equation (9):

$$\alpha_t = \sqrt{\frac{M_{N_2}}{M_{He}}} \tag{9}$$

where α_t is the theoretical selectivity, M_{N_2} is the molecular weight of nitrogen, and M_{He} is the molecular weight of helium. In the mixed-flow domain, the contributions are from Knudsen diffusion and viscous flow, wherein the viscous flow falls in the nonselective domain. Equation (10) shows the relationship between theoretical and experimental selectivity:

$$\alpha_E = \alpha_t k \tag{10}$$

where, α_E is experimental selectivity and k is the contribution from Knudsen diffusion.

4. Results and discussion

4.1. Dose deposition studies using Monte Carlo simulations

Table 1 shows the details of the ion beams and the corresponding range in the PET film calculated by SRIM code. It was observed that with the increase in the energy of the beam for Si ion from 70 to 90 MeV, the energy deposited per nucleon increases from 2.5 to 3.2 MeV, while the range of ion increases from 28.9 to 38.5 µm. Thus, there is a direct correlation between the range of the ions and their energy. The higher the energy of the particle, the lesser is its interaction with the film, and hence it is able to cover a higher distance in the film before losing its energy. A similar trend has been observed for Cl ions. It can be seen that the range of the ions in all cases is higher than the thickness of the film.

Figure 4 shows the distribution of absorbed dose in the film as a function of thickness. It can be observed

Table 1. Mean absorbed dose and the mean displacement per atom in the PET film.

Ion	Energy [MeV]	Energy/nucleon [MeV]	Range of the ion calculated by SRIM code [µm]
Si	70	2.5	28.9
Si	90	3.2	38.5
Cl	84	2.4	28.4
Cl	100	2.9	33.6
Cl	115	3.3	39.8

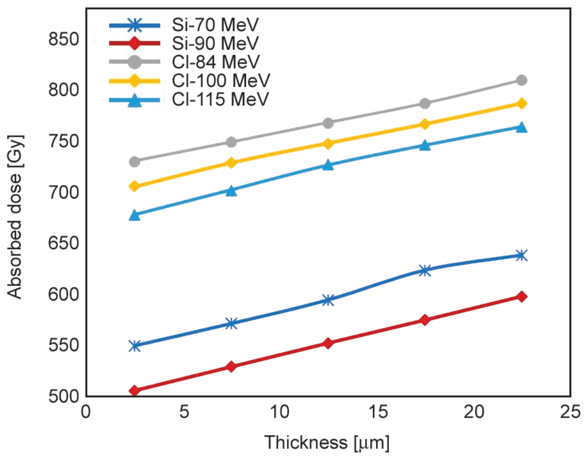

Figure 4. Absorbed dose as a function of the thickness of the film.

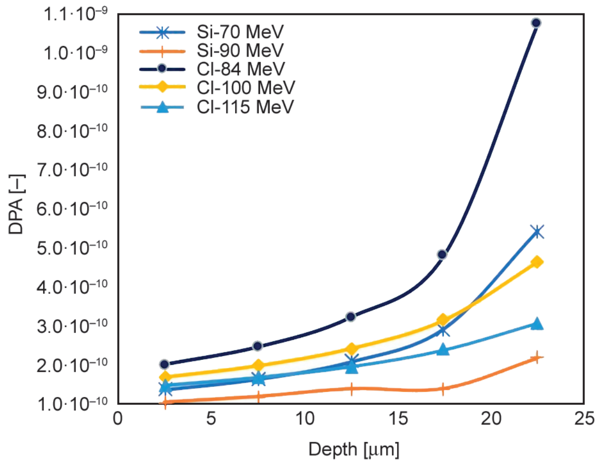

Figure 6. DPA as a function of the thickness of the film.

that the absorbed dose increases with the increase in thickness of the film and decreases with an increase in the energy of an incident ion. This is because the range of all the ions is higher than the thickness of the film. Hence, with the increase in the thickness of the film, the interaction of ions also increases, and more energy is deposited in the film. The decrease in absorbed dose with an increase in the energy of the beam is because as the energy of the particle increases, its speed also increases, which results in a lower interaction of particles with the polymer.

Figure 5 shows the mean absorbed dose as a function of the energy of the ion. It can be seen that with the increase in ion energy, the absorbed dose decreases. Figure 6 shows the DPA at various depths in the film, and it can be observed that DPA increases with the depth. With the increase in depth, the ion loses its energy, and as the energy of the ion reduces, its interaction with film increases due to higher interaction time, and this leads to higher DPA. Figure 7 shows the mean DPA as a function of incident ion energy. The DPA decreases as the energy of the ion increases. This is because, with the increase in the energy of ions, the interaction of the ion with the film decreases. This is also confirmed and validated experimentally, as is evident from the results discussed in Section 4.6. In the case of Si irradiation, it was observed that the etching rate had increased nearly by a factor of 1.5, with an increase in energy from 70 to 90 MeV. A similar observation was also made in the case of the Cl beam. It is due to the higher degree of damage caused by the high-energy ions in the polymer matrix. Based on the results, it was observed that DPA was minimum in the case of Si (90 MeV), and at the same time, it has a higher range. Hence, for experimental studies, a 90 MeV beam of Si-28 was used for the irradiation of the PET film. However, the etching rate at optimized conditions was studied for membranes exposed to both Si and Cl ion beams of different energies.

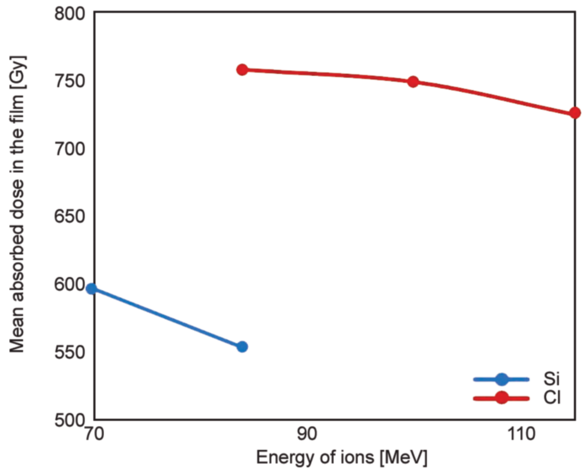

Figure 5. Absorbed dose as a function of ion energy.

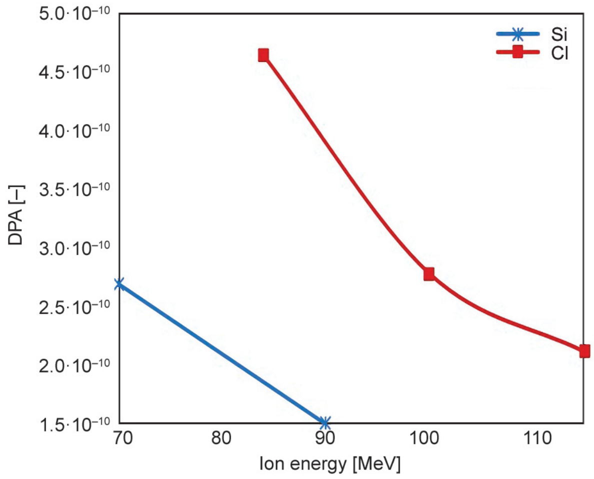

Figure 7. Mean DPA as a function of ion energy.

4.2. Effect of concentration of etching solution on weight loss of PET film

Figure 8 shows the effect of the concentration of NaOH solution on weight loss of control and irradiated polymers (irradiated with Si-90 MeV) at 60 °C. The NaOH interacts with –COO groups of PET which get hydrolyzed during etching. It is observed that the weight loss of both (control and irradiated) films increases with the concentration of etchant, but the rate of increase in weight loss is higher when the concentration of alkali is increased from 3 to 6 N. However, when the concentration increases from 6 to 10 N, the rate of increase in weight loss is reduced. It is also observed that the difference in weight loss in irradiated and unirradiated polymers first increase with an increase in the concentration of etchant from 3 to 6 N, and thereafter it remains nearly constant. Therefore, for further studies, the concentration of etchant was fixed as 6 N.

4.3. Effect of temperature of etching solution on weight loss of PET film

Figure 9 shows the effect of temperature on weight loss of control and irradiated polymers (with Si-90 MeV) with a 6 N concentration of NaOH. It was observed that the rate of etching of both irradiated and unirradiated polymers increases with the increase in temperature, since the etching of PET is a chemical reaction, and the rate of chemical reaction increases with temperature. However, it is observed that the difference between weight loss of irradiated and unirradiated polymers increases sharply with an increase in temperature from 50 to 60 °C, while it becomes nearly constant thereafter. Hence, for subsequent studies, the temperature was fixed at 60 °C. Hydrolysis of PET is a first-order reaction [46]. Usually, in first-order chemical reactions, the etching rate increases by a factor of ~2–3 for an increase in temperature by 10 °C. Therefore, in technical processes, high throughput necessitates high etching temperatures. Alternating the etching temperature can aid in obtaining ion tracks with high aspect ratios and large diameters. At room temperature, diffusion processes can be faster than chemical reactions of the etchant within the polymer.

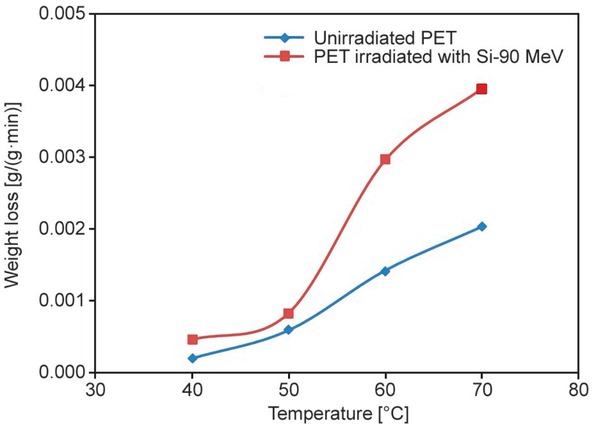

Figure 9. Effect of temperature on weight loss of unirradiated and irradiated PET film in 6 N NaOH.

4.4. Effect of ultrasonication during etching on weight loss of PET film

Figure 10 shows the effect of ultrasonication on the etching rate (weight loss) of irradiated and unirradiated PET films. It can be observed that the rate of etching of control and irradiated polymers increases with ultrasonication. Also, the difference in weight loss of unirradiated and irradiated polymers is higher

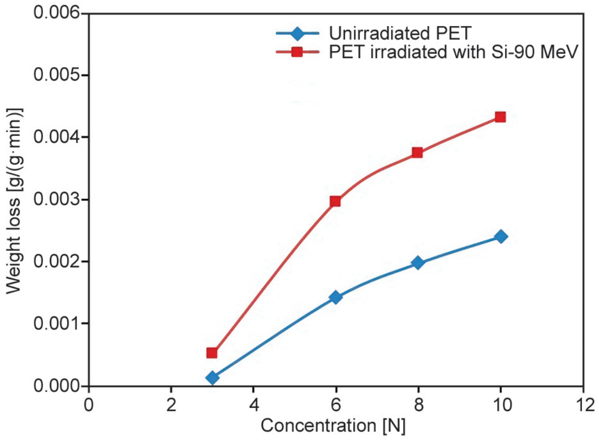

Figure 8. Weight loss of unirradiated and irradiated PET film *v/s* concentration of NaOH solution at a temperature of 60 °C.

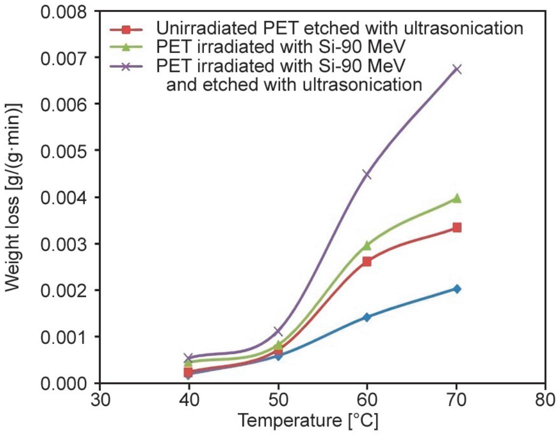

Figure 10. Effect of ultrasonication during etching on weight loss of PET film.

in the case of ultrasonication, compared to the films that were etched without ultrasonication.

4.5. Effect of UV irradiation before etching

Tables 2 and 3 summarize the effect of UV irradiation on the weight of polymer samples with one as well as both sides of the membranes exposed to UV radiation, respectively. It is observed that there is no weight loss in samples after UV treatment.

Figure 11 shows that the weight loss during etching (after exposure to UV radiation) is more in the case of irradiated membranes as compared to unirradiated membranes. Hence, UV treatment was found to be necessary to enhance the etching rate. This is because UV irradiation causes photo-oxidation in the polymer matrix, leading to a higher etching rate. It was also observed that UV treatment on both sides of PET film has a higher deteriorating effect, compared to that in the case of single-sided UV exposure.

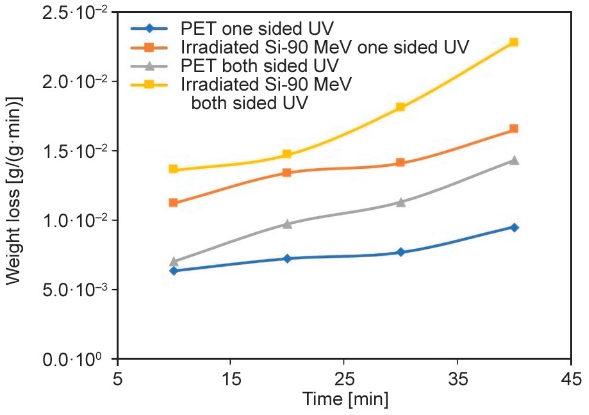

Figure 11. AFM image of unirradiated PET film.

4.6. Effect of energy of irradiation beam on weight loss of PET film

Table 4 shows the effect of the energy of irradiating beams (Si and Cl) on the etching rate of irradiated polymers. In the case of Si irradiation, it is observed that the etching rate has increased nearly by a factor of 1.5 with an increase in energy from 70 to 90 MeV. A similar observation was also made in the case of the Cl beam. It is due to the higher degree of damage caused by the high-energy ions in the polymer matrix. The simulation studies also confirmed that the absorbed dose increases with an increase in the energy of ions. A higher absorbed dose leads to a higher degree of damage to the polymer.

Table 4. Effect of incident beam energy on etching rate of PET film.

Ion	Energy [MeV]	Weight loss [g/(g·min)]
Si	70	$1.3858\cdot10^{-3}$
Si	90	$2.3102\cdot10^{-3}$
Cl	84	$2.6210\cdot10^{-3}$
Cl	100	$2.9120\cdot10^{-3}$
Cl	115	$3.5340\cdot10^{-3}$

Table 2. Effect of UV irradiation (one side of polymer film exposed) on the weight of PET film.

Sample	Time [min]	Initial weight [g]	Final weight after UV treatment [g]
PET	10	0.0567	0.0567
PET	20	0.0597	0.0597
PET	30	0.0484	0.0484
PET irradiated with Si-90 MeV	10	0.0684	0.0684
PET irradiated with Si-90 MeV	20	0.0629	0.0629
PET irradiated with Si-90 MeV	30	0.0513	0.0513

Table 3. Effect of UV irradiation (both sides of polymer film exposed) on the weight of PET film.

Sample	Time [min]	Initial weight [g]	Final weight after UV treatment [g]
PET	10	0.0618	0.0618
PET	20	0.0498	0.0498
PET	30	0.0759	0.0759
PET irradiated with Si-90 MeV	10	0.0543	0.0543
PET irradiated with Si-90 MeV	20	0.0380	0.0380
PET irradiated with Si-90 MeV	30	0.0578	0.0578

4.7. Characterization of PET films

4.7.1. Surface roughness studies

Figures 12 to 14 show the AFM images of control, irradiated, and etched polymer samples, respectively. It is observed that surface roughness has increased after irradiation and etching. The increase in the density of bright spots after irradiation is an indication of an increase in surface roughness. The average surface roughness has increased from ~3 to ~6 nm after irradiation with Si-90 MeV, while it increases to ~53 nm after being etched. The image has been analyzed with ImageJ software and its pore size determination. The pore size was found to be ~300 nm.

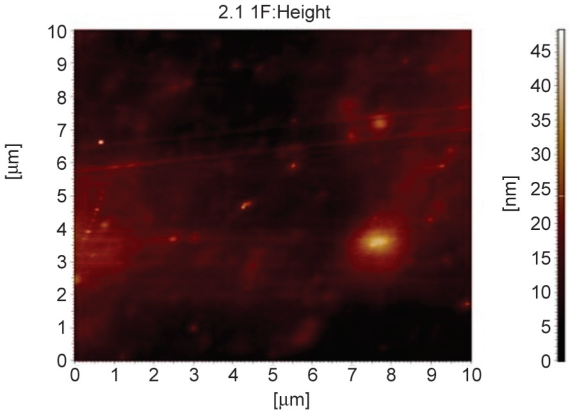

Figure 12. AFM image of unirradiated PET film.

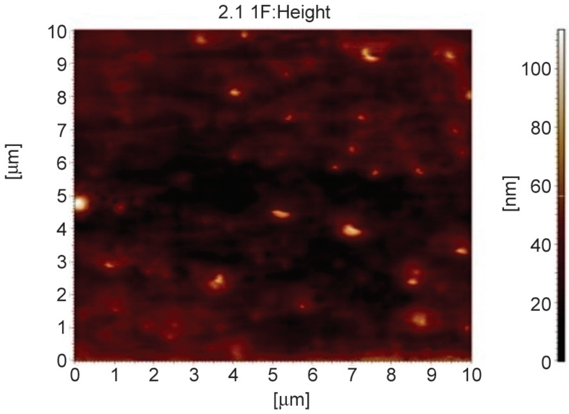

Figure 13. AFM image of irradiated PET by Si-90 MeV.

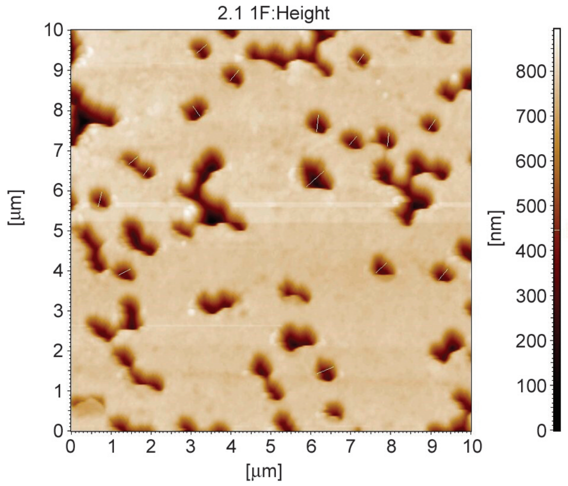

Figure 14. AFM image of etched PET (60 °C, 6N NaOH, with UV and ultrasonication).

4.7.2. Morphological studies

Figure 15 shows a typical SEM image of PET film etched at 60 °C in 6 N NaOH with UV irradiation and ultrasonication. It is clear from the SEM image that there is a good pore density. The image was further analyzed using ImageJ software to determine the pore size, and it was found that the membrane has an average pore size of ~150 nm. SEM image clearly indicates the presence of distinct pores in the membrane, and pore merger is not observed except in very few locations. This is also confirmed by the AFM analysis discussed earlier.

4.7.3. Thermal analysis

The TGA analysis of different samples is shown in Figure 16. It shows that the weight loss increased with irradiation (with Si-90 MeV and UV), indicating a decrease in the thermal stability of the polymer due to irradiation. However, the onset of weight loss is at around 375 °C, which shows that thermal degradation of the membrane takes place after 375 °C. It can be observed from the zoomed-in figures (Figure 16b–16d) that a higher weight loss occurs in the case of the irradiated membrane as compared to the unirradiated membrane. In the case of an unirradiated membrane, a weight loss of ~60% takes place at decomposition, while the weight loss for irradiated samples is ~70%.

The DSC analysis of different samples is shown in Figure 17. It is observed that the area of peak in the case of irradiated (Si-90 MeV and/or UV) polymers

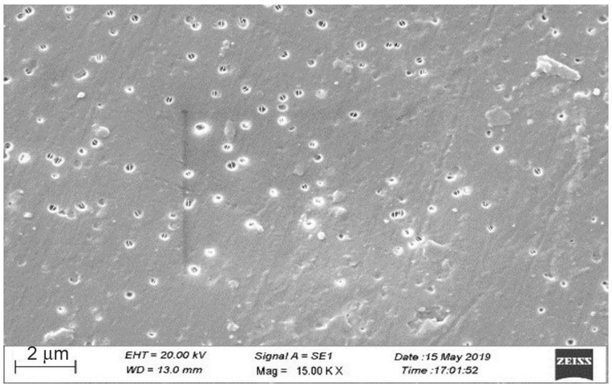

Figure 15. SEM image of etched PET (60 °C, 6 N NaOH, with UV and ultrasonication).

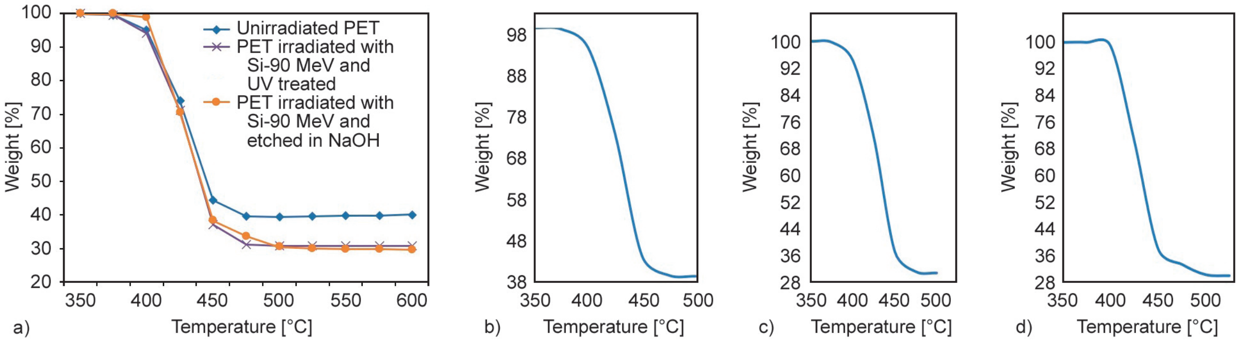

Figure 16. TGA analysis of PET membrane samples and zoomed-in curves for decomposition peak. a) PET samples, b) unirradiated PET c) PET irradiated with Si-90 MeV and UV treatment. d) PET iradiated with Si-90 MeV and etched in NaOH.

is larger than that of the unirradiated ones since the decomposition kinetics of PET increases with irradiation due to chain scission of the polymer. With an increase in the kinetics of decomposition, the energy gets released in a shorter span of time, leading to a sharper peak. A drop in heat flow between 50 and 100 °C may be due to the glass transition of polymer followed by an increase (between 100–150 °C) in heat transfer due to cold crystallization and a final drop (between 200–250 °C) due to melting. As compared to unirradiated and untreated PET, DSC curves of both UV and NaOH-treated PET samples show enhanced crystallization, possibly due to chemical or UV irradiation-induced degradation in the polymer structure. Figure 17 also shows distinct peaks for melting, glass transition, and crystallinity at temperatures of ~250, 85, and 186 °C respectively.

The degree of relative crystallinity (X_c) of PET is calculated from the enthalpies of fusion (melting peaks) using the Equation (11):

$$X_\mathrm{c} = \frac{\Delta H_\mathrm{f}}{w \cdot \Delta H_\mathrm{f,100}} \cdot 100 \tag{11}$$

where ΔH_f and $\Delta H_\mathrm{f,100}$ are the heat of fusion (melting) as measured for a sample and the average heat of fusion of 100% crystalline PET (or in this case, as-procured PET being the base material to see relative changes), w is the weight fraction of polymer which is 1 in this case.

From Equation (11), it was found that after etching, the relative crystallinity of the polymer increased approximately 3 times, which was also observed through XRD analysis. The heat of fusion was obtained by calculating the area under the melting peaks in the curves (shown in Figure 17). It was found that the area under the curve for unirradiated, irradiated, and etched membranes are 50, 100, and 150 mW·°C/mg. UV treatment increases the relative crystallinity of the membrane by forming an ordered arrangement of molecules in the film [47]. The increase in relative

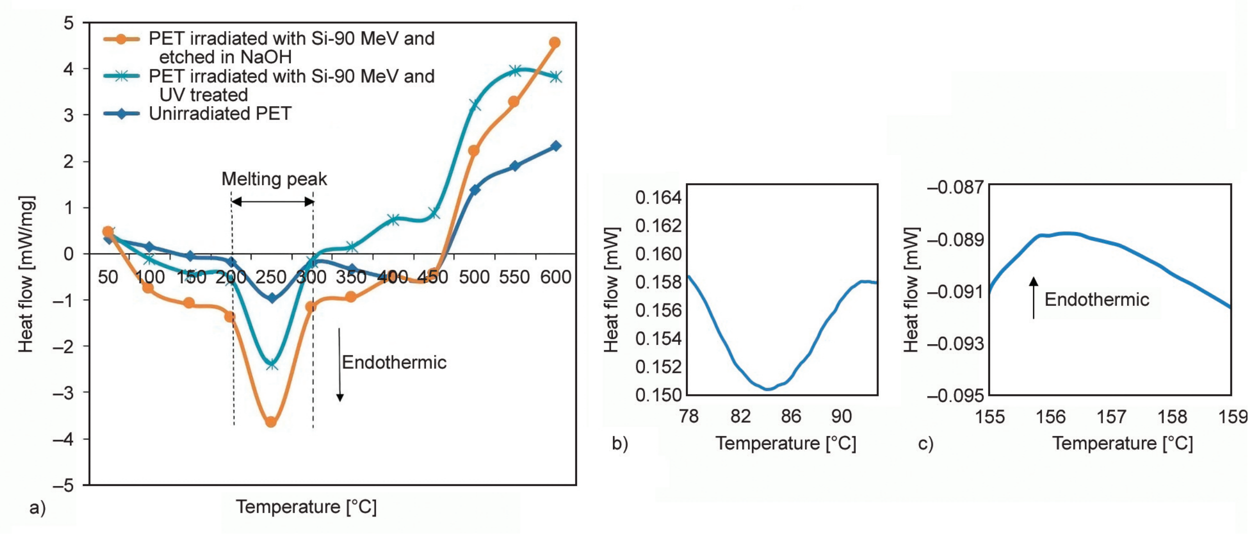

Figure 17. DSC analysis of PET samples. a) Melting peak, b) glass transition peak, c) crystallinity peak.

crystallinity after etching may be due to the dissolution of less crystalline phases during the etching process.

4.7.4. XRD analysis

XRD analysis of different samples is shown in Figure 18. It is observed from the figure that there is an increase in the relative crystallinity of the sample with irradiation and etching. The same phenomenon has been observed in DSC analysis as well. FWHM (full width at half maximum) calculation was carried out for the XRD curves, and it was found that for the PET sample, the FWHM value is ~1.45; for the irradiated membrane, the FWHM is ~1.4, and for etched membrane, the FWHM is ~0.62. Hence, it can be concluded that crystallinity has increased after etching.

4.8. Pure water permeation studies

No flow of water was observed on permeate side at a trans-membrane pressure of 1 bar which may be due to the small pore size with low porosity. A similar observation has been reported in the literature [48] for a membrane of pore size of around 0.25 µm which has not shown any flux of water till a pressure of 1.5 bar. However, in this case, the pore size is less than 0.1 µm, and hence, no water permeation was observed at a pressure of 1 bar.

4.9. Gas permeation studies

Table 5 shows the variation of selectivity of etched membranes with pressure. The selectivity decreases from 2.4 to 1.6 with an increase in pressure from 1 to 3 bar. This is due decrease in the mean free path with an increase in pressure. Hence, the ratio of the mean free path to the diameter of the pore decreases, which leads to a shift of permeation flow from Knudsen diffusion to the viscous flow regime. The viscous flow is a non-selective regime, and hence the selectivity decreases. Table 6 shows the gas composition of the product stream for 20% He-80% N_2 gas mixture in feed. It is observed that the selectivity is reduced when mixed gas is used instead of pure gas, due to competitive adsorption-diffusion between two species [48].

The permeance of the etched PET membrane was calculated using Equation (8). The permeance of helium was found to be higher than nitrogen due to its lower molecular weight. At the same time, its theoretical selectivity calculated by Equation (9) was found to be 2.64. The experimental selectivity was found to be 2.4 (less than theoretical selectivity, which is the inverse ratio of under root of molecular weights [47]). This indicates that the flow domain is a mixed one and there is a contribution of the nonselective viscous domain. Table 7 shows the permeance of the membrane for He and N_2. The studies confirmed that these membranes could be effectively used for the separation of helium from helium-nitrogen mixture in industries.

Figure 19 shows the extent of the contribution of the Knudsen diffusion regime in the permeation with pressure. It is clear from the figure that the contribution of

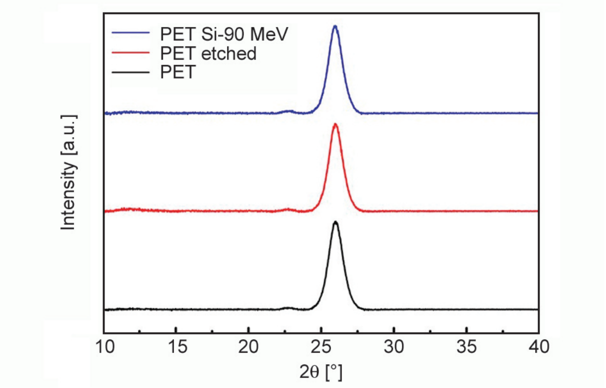

Figure 18. XRD analysis of PET samples.

Table 5. Variation of selectivity of etched membranes (60 °C, 6 N NaOH, with UV and ultrasonication) with pressure.

Pressure [bar]	Selectivity (He/N_2)
1	2.4
2	1.8
3	1.6

Table 6. Composition of product stream from etched membranes for 20% He-80% N_2 gas mixture with pressure.

Pressure [bar]	He [%]	N_2 [%]
1	29.6	70.4
2	23.0	77.0
3	20.0	80.0

Table 7. Permeance of membrane (60 °C, 6 N NaOH, with UV and ultrasonication) for He and N_2.

Gas	Permeance [mol/(m^2·s·Pa)]
He	$3.35\cdot10^{-7}$
N_2	$1.40\cdot10^{-7}$

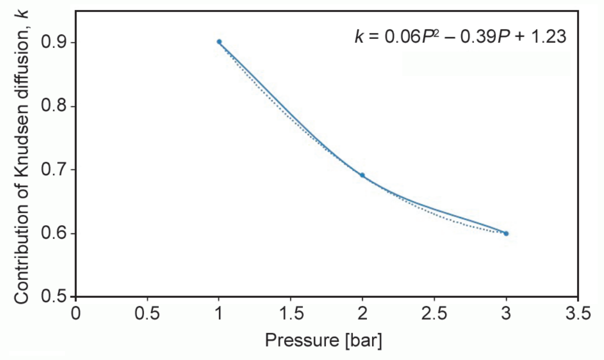

Figure 19. Variation of Knudsen diffusion contribution with pressure.

Knudsen diffusion decreases with an increase in pressure.

As the pressure increases, the mean free path length decreases, reducing the ratio of the mean free path length to the pore diameter. This drop in contribution from the Knudsen domain is not gradual, because the membrane has a pore size distribution. It follows a quadratic polynomial with the equation: $0.06P^2 - 0.39P + 1.23$, where P is the pressure. Based on the results obtained in terms of permeance and selectivity of membrane for He/N_2 system, it is observed that the membrane has high permeability (~2500 barrer) with relatively low selectivity (~2), and in the Robeson trade-off line, its position lies in the low selectivity and high permeability zone. However, its permeability is higher than the 1991 upper bound. The studies confirmed that PET track etched membranes could be deployed in the industry for the separation and recovery of helium from the helium-nitrogen system. As it is confirmed that the flow domain is in the Knudsen diffusion regime, the same membrane, if used for He/CH_4 separation, will give a selective separation of He from CH_4 due to difference in molecular weights of both the components. An ideal selectivity of ~4 can be achieved for this gas mixture (with Knudsen diffusion as the dominant transport mechanism). However, in the realistic system, the selectivity will be lower than the ideal selectivity.

5. Conclusions

This is the first of its kind study undertaken for the development of track-etched membranes for the separation of helium from nitrogen. Monte Carlo simulations of membrane irradiation with ion beams were carried out using the FLUKA code. It was found that the absorbed dose increases with an increase in the thickness of the film and decreases with an increase in the energy of the incident ion. The simulation studies also showed that the DPA increases with the depth in the film and the energy of the ions. Based on the results, it was observed that DPA was minimum, and the range was higher in the case of Si-90 MeV. Hence, for experimental studies, a 90 MeV beam of Si-28 was used for the irradiation of the PET film. The etching rate at optimized conditions was studied for membranes exposed to both Si and Cl ion beams of different energies. The effect of parameters, such as temperature, the concentration of NaOH, UV radiation, and ultrasonication on the etching rate was studied for the synthesis of PET track-etched membrane. The parameters where the difference in etching rate of the irradiated and unirradiated polymer was found to be maximum were taken as optimum. The optimum set of operating conditions was found to be 6 N NaOH as an etching agent at a temperature of 60 °C with ultrasonication and UV irradiation for 10 minutes on both sides of the polymer film. It was found that both ultrasonication and UV treatment leads to an increase in the etching rate of both irradiated and unirradiated polymer films. The surface roughness and degradation kinetics of the sample also increases with irradiation and etching. The gas permeation studies of in-house fabricated membrane offered a He permselectivity of up to 2.5, which is close to Knudsen diffusion-based selectivity. The studies confirmed that PET track etched membranes can be deployed in industry for separation and recovery of helium from helium-nitrogen system.

Acknowledgements

The authors would like to acknowledge and thank Mr. P. P. Surve, Mr. R. B. Bramhane and Mr. A. K. Singha from Desalination and Membrane Technology Division, BARC, Mr. Prince Bagthariya from Chemical Engineering Department, Om Engineering College, for their valuable contribution in this work.

References

[1] Dai Z., Deng J., He X., Scholes C. A., Jiang X., Wang B., Guo H., Ma Y., Deng L.: Helium separation using membrane technology: Recent advances and perspectives. Separation and Purification Technology, **274**, 119044 (2021). https://doi.org/10.1016/j.seppur.2021.119044

[2] Chhandak A. K., Israni R., Trivedi A.V.: A review on the real life applications of helium. Journal of Current Microbiology and Applied Sciences, **6**, 533–593 (2017). https://doi.org/10.20546/ijcmas.2017.606.063

[3] Scholes C. A., Ghosh U. K.: Review of membranes for helium separation and purification. Membranes, **7**, 9–22 (2017). https://doi.org/10.3390/membranes7010009

[4] Pereira E. B., Adams J. A. S.: Helium production in natural gas reservoirs. Geophysical Research Letters, **9**, 87–90 (1982). https://doi.org/10.1029/GL009i001p00087

[5] Rufford T. E., Chan K. I., Huang S. H., May E. F.: A review of conventional and emerging process technologies for the recovery of helium from natural gas. Adsorption Science and Technology, **32**, 49–72 (2014). https://doi.org/10.1260/0263-6174.32.1.49

[6] Xiong L., Peng N., Liu L., Gong L.: Helium extraction and nitrogen removal from LNG boil-off gas. IOP Conference Series: Materials Science and Engineering, **171**, 12003–12010 (2017). https://doi.org/10.1088/1757-899X/171/1/012003

[7] Castel C., Favre E.: Membrane separations and energy efficiency. Journal of Membrane Science, **548**, 345–357 (2018). https://doi.org/10.1016/j.memsci.2017.11.035

[8] Baker R. W.: Membrane technology and applications. Wiley, Hoboken (2004).

[9] Ismail A. F., Khulbe K. C., Matsuura T.: Gas separation membranes. Springer, Cham (2015). https://doi.org/10.1007/978-3-319-01095-3

[10] Stewart M., Arnold K.: Gas sweetening and processing field manual. Gulf Professional Publishing, Boston (2011).

[11] Ismail A. F., Matsuura T.: Sustainable membrane technology for energy, water, and environment. Wiley, Hoboken (2012).

[12] Ball P.: Scale-up and scale-down of membrane-based separation processes. Membrane Technology, **2000**, 10–13 (2000). https://doi.org/10.1016/S0958-2118(00)86634-3

[13] Alqaheem Y., Alomair A., Vinoba M., Pérez A.: Polymeric gas-separation membranes for petroleum refining. International Journal of Polymer Science, **2017**, 4250927 (2017). https://doi.org/10.1155/2017/4250927

[14] George G., Bhoria N., AlHallaq S., Abdala A., Mittal V.: Polymer membranes for acid gas removal from natural gas. Separation and Purification Technology, **158**, 333–356 (2016). https://doi.org/10.1016/j.seppur.2015.12.033

[15] Figoli A., Cassano A., Basile A.: Membrane technologies for biorefining. Woodhead, Cambridge (2016).

[16] Merkel T., Pinnau I.: Organic-inorganic nanocomposite membranes for molecular separation processes. in 'Nanostructure control of materials' (eds.: Hannink R. H. J., Hill A. J.) Woodhead Publishing, Cambridge, 76–96 (2006). https://doi.org/10.1533/9781845691189.76

[17] Low Z-X., Budd P. M., McKeown N. B., Patterson D. A.: Gas permeation properties, physical aging, and its mitigation in high free volume glassy polymers. Chemical Reviews, **118**, 5871–5911 (2018). https://doi.org/10.1021/acs.chemrev.7b00629

[18] Baker R. W., Low B. T.: Gas separation membrane materials: A perspective. Macromolecules, **47**, 6999–7013 (2014). https://doi.org/10.1021/ma501488s

[19] Zhou H., Jin W.: Membranes with intrinsic microporosity: Structure, solubility, and applications. Membranes, **9**, 3 (2018). https://doi.org/10.3390/membranes9010003

[20] Soleimany A., Karimi-Sabet J., Hosseini S. S.: Experimental and modeling investigations towards tailoring cellulose triacetate membranes for high performance helium separation. Chemical Engineering Research and Design, **137**, 194-212 (2018). https://doi.org/10.1016/j.cherd.2018.07.011

[21] Akbari A., Karimi-Sabet J., Mohammad G. S.: Polyimide based mixed matrix membranes incorporating Cu-BDC nanosheets for impressive helium separation. Separation and Purification Technology, **253**, 117430 (2020). https://doi.org/10.1016/j.seppur.2020.117430

[22] Liu X., Chang X., Zhu L., Li X.: High-efficiency helium separation through g-C_2O membrane: A theoretical study. Computational Materials Science, **157**, 1–5 (2019). https://doi.org/10.1016/j.commatsci.2018.10.022

[23] Savoji H., Rana D., Matsuura T., Soltanieh M., Tabe S.: Novel surface modifying macromolecules (SMMs) blended polysulfone gas separation membranes by phase inversion technique. Journal of Applied Polymer Science, **124**, 2287–2299 (2012). https://doi.org/10.1002/app.34809

[24] Savoji H., Rana D., Matsuura T., Soltanieh M., Tabe S.: Influence of novel surface modifying macromolecules and coagulation media on the gas permeation properties of different polymeric gas separation membranes. Journal of Applied Polymer Science, **124**, 2300–2310 (2012). https://doi.org/10.1002/app.35281

[25] Rana D., Matsuura T.: Oxygen–nitrogen separation. in 'Encyclopedia of membrane science and technology' (eds.: Hoek E. M., Tarabara V. V.) Wiley, Hoboken, Vol. 3, 1–26 (2013). https://doi.org/10.1002/9781118522318.emst099

[26] Fen C-S., Liang W., Hsiesh P., Huang Y.: Knudsen and molecular diffusion coefficients for gas transport in unconsolidated porous media. Soil Science Society of America Journal, **75**, 456-467 (2011). https://doi.org/10.2136/sssaj2010.0122

[27] Gitis V., Rothenberg G.: Ceramic membranes: New opportunities and practical applications. Wiley, Weinheim (2016). https://doi.org/10.1002/9783527696550

[28] Spiridonov V. S., Belov S. V., Kirikova O. V.: Calculation of mean pore size in porous materials. Journal of Engineering Physics, **53**, 1169–1172 (1987). https://doi.org/10.1007/BF00872449

[29] Shen J. Z., Kosmač T.: Advanced ceramics for dentistry. Elsevier, Waltham (2014). https://doi.org/10.1016/C2011-0-07169-7

[30] Tan X., Rodrigue D.: A review on porous polymeric membrane preparation. Part I: Production techniques with polysulfone and poly (vinylidene fluoride). Polymers, **11**, 1160–1199 (2019). https://doi.org/10.3390/polym11071160

[31] Leclerc M., Gauvin R.: Functional materials: For energy, sustainable development and biomedical sciences. de Gruyter, Berlin (2014). https://doi.org/10.1515/9783110307825

[32] Yu A. B., Standish N.: Characterisation of non-spherical particles from their packing behaviour. Powder Technology, **74**, 205–213 (1993). https://doi.org/10.1016/0032-5910(93)85029-9

[33] Korolkov I. V., Mashentseva A. A., Güven O., Gorin Y. G., Zdorovets M. V.: Protein fouling of modified microporous PET track-etched membranes. Radiation Physics and Chemistry, **151**, 141–148 (2018). https://doi.org/10.1016/j.radphyschem.2018.06.007

[34] Ensinger W., Sudowe R., Brandt R., Neumann R.: Gas separation in nanoporous membranes formed by etching ion irradiated polymer foils. Radiation Physics and Chemistry, **79**, 204–207 (2010). https://doi.org/10.1016/j.radphyschem.2009.08.045

[35] Mchedlishvili B. V., Berezkin V. V., Vasil'ev A. B., Vilenskiĭ A. I., Zagorskiĭ D. L., Miterev A. M., Oleĭnikov V. A.: Problems and prospects of development of nanomembrane technology. Crystallography Reports, **51**, 850–862 (2006). https://doi.org/10.1134/S1063774506050166

[36] Kamakshi, Kumar R., Saraswat V. K., Kumar M., Awasthi K.: Palladium nanoparticle binding in functionalized track etched PET membrane for hydrogen gas separation. International Journal of Hydrogen Energy, **42**, 16186–16194 (2017). https://doi.org/10.1016/j.ijhydene.2017.05.040

[37] Ferain E., Legras R.: Templates for engineered nano-objects for use in microwave, electronic devices and biomedical sensing application. Nuclear Instruments and Methods in Physics Research Section B: Beam Interactions with Materials and Atoms, **267**, 1028–1031 (2009). https://doi.org/10.1016/j.nimb.2009.02.013

[38] Xavier S., Mátéfi-Tempfli S., Ferain E., Purcell S., Enouz-Vedrenne S., Gangloff L., Minoux E., Hudanski L., Vincent P., Schnell J-P.: Stable field emission from arrays of vertically aligned free-standing metallic nanowires. Nanotechnology, **19**, 215601 (2008). https://doi.org/10.1088/0957-4484/19/21/215601

[39] Fleischer R. L., Price P. B., Walker R. M.: Nuclear tracks in solids: Principles and applications. Mineralogical magazine, **42**, 306–307 (1975). https://doi.org/10.1180/minmag.1978.042.322.40

[40] Korolkov I. V., Gorin Y. G., Yeszhanov A. B., Kozlovskiy A. L., Zdorovets M. V.: Preparation of PET track-etched membranes for membrane distillation by photo-induced graft polymerization. Materials Chemistry and Physics, **205**, 55–63 (2018). https://doi.org/10.1016/j.matchemphys.2017.11.006

[41] Makkonen-Craig S. A., Yashina K., Paronen M.: Track-etched ultrafiltration polymer membranes produced by light ion irradiation. Arcada Working Papers, **2014**, 1–13 (2018).

[42] Hosseini S., Taheri S., Zadhoush A., Mehrabani-Zeinabad A.: Hydrolytic degradation of poly(ethylene terephthalate). Journal of Applied Polymer Science, **103**, 2304–2309 (2007). https://doi.org/10.1002/app.24142

[43] Venkatachalam S., Nayak S. G., Labde J. V., Gharal P. R., Rao K., Kelkar A. K.: Degradation and recyclability of poly(ethylene terephthalate). in 'Polyster' (ed.: Saleh H.) IntechOpen, London (2012). https://doi.org/10.5772/48612

[44] Böhlen T. T., Cerutti F., Chin M. P. W., Fassò A., Ferrari A., Ortega P. G., Mairani A., Sala P. R., Smirnov G., Vlachoudis V.: The FLUKA code: Developments and challenges for high energy and medical applications. Nuclear Data Sheets, **120**, 211–214 (2014). https://doi.org/10.1016/j.nds.2014.07.049

[45] Yang W., Liu R., Li C., Song Y., Hu C.: Hydrolysis of waste polyethylene terephthalate catalyzed by easily recyclable terephthalic acid. Waste Management, **135**, 267–274 (2021). https://doi.org/10.1016/j.wasman.2021.09.009

[46] Park S., Kwon E., Park Y.: Effect of localized UV irradiation on the crystallinity and electrical properties of dip-coated polythiophene thin films. RSC Advances, **10**, 34130–34136 (2020). https://doi.org/10.1039/D0RA06339H

[47] Chittrakarn T., Bhongsuwan T., Wanichapichart P., Nuanuin P., Chongkum S., Khonduangkaew A., Bordeepong S.: Nuclear track-etched pore membrane production using neutrons from the Thai research reactor TRR-1/M1. Songklanakarin Journal of Science and Technology, **24**, 863–870 (2002).

[48] Hu Y., Shiotsuki M., Sanda F., Freeman B. D., Masuda T.: Synthesis and properties of indan-based polyacetylenes that feature the highest gas permeability among all the existing polymers. Macromolecules, **41**, 8525–8532 (2008). https://doi.org/10.1021/ma801845g